EOS MLS Forward Model Polarized Radiative Transfer for Zeeman-Split Oxygen Lines

Michael J. Schwartz, William G. Read, W. Van Snyder

Abstract— This work supplements the EOS MLS clear-sky unpolarized forward model [1] with algorithms for modeling polarized emission from the Zeeman-split 118.75-GHz O_2 spectral line. The model accounts for polarization-dependent emission and for correlation between polarizations with complex, 2x2 intensity and absorption matrices. The oxygen line is split into three Zeeman components by the interaction of oxygen's electronic spin with an external magnetic field, and the splitting is of order ± 0.5 MHz in a typical geomagnetic field. Zeeman splitting is only significant at pressures low enough that collisional broadening ($\sim$1.6 MHz/hPa) is not very large by comparison. The polarized forward model becomes significant for MLS temperature retrievals at pressure below 1.0 hPa and is crucial at pressures below $\sim$0.03 hPa. Interaction of the O_2 molecule with the radiation field depends upon the relative orientation of the radiation polarization mode and the geomagnetic field direction. The model provides both limb radiances and the derivatives of these radiances with respect to atmospheric temperature and composition, as required by MLS temperature retrievals. EOS MLS views the atmospheric limb at 118.75 GHz with a pair of linear-cross-polarized, 100-kHz-resolution, 10-MHz-wide spectrometers. The antennas of the associated receivers are scanned to view rays with tangent heights from the Earth's surface to 0.001 hPa. Comparisons of the modeled MLS radiances with measurements show generally good agreement in line positions and strengths, however residuals in the line centers at the highest tangent heights are larger than desired and still under investigation.

Index Terms— Zeeman, EOS Aura, MLS, Forward Model

I. Introduction

The EOS Microwave Limb Sounder (MLS) instrument [2], one of four instruments on the Aura spacecraft launched on July 15, 2004, measures thermal millimeter-wave emission from the Earth's limb. Atmospheric composition and temperature from 316 hPa to 0.001 hPa ($\sim$8 km to $\sim$95 km) are inferred from these measurements. At the highest-altitude pointings of the MLS limb scan, the primary source of temperature information is near the line center of the 118-GHz oxygen line. This line splits into three components due to the Zeeman interaction of oxygen's electronic spin with the geomagnetic field; the upper and lower components (labeled $\pm\sigma$) are shifted ± 0.5 MHz from the central (π) component in a typical mid-latitude, 35-μT geomagnetic field. Absorption and emission by these three Zeeman components generally depends upon the orientation of the external magnetic field with respect to the direction of radiation propagation and upon the radiation polarization.

M.J. Schwartz, W.G. Read and W.V. Snyder are with the Jet Propulsion Laboratory, 4800 Oak Grove Dr. Pasadena, CA 91109

At pressures higher than $\sim$10 hPa, Zeeman splitting is negligible compared to the $\sim$1.6 MHz/hPa collisional broadening, and the three components add in such a way that absorption is isotropic at all frequencies. However, higher in the atmosphere as line widths approach the thermal Doppler width ($\sim$0.21 MHz full width at half maximum at 200 K), line widths become comparable to Zeeman splitting, and the radiative transfer becomes polarization-dependent. Temperature information is contained in the line-centers of the Zeeman components at the highest-altitude tangent pointings. The emitted radiances from these components can vary by 180 K or more with changes in geomagnetic field orientation as components shift and appear or vanish, so the retrieval [3] requires both a high-resolution spectrometer capable of resolving the component lines and a radiative transfer model which accounts for orientation and polarization dependence. Errors in retrieved temperature have follow-on effects in atmospheric constituent retrievals, both in that geometric pointing and retrieval pressure surfaces are linked through the assumption of hydrostatic balance, and in that radiances on unsaturated spectral lines are proportional to both temperature as well as absorber abundance.

The EOS MLS instrument has two 100-kHz-resolution digital autocorrelator spectrometers (DACS) attached to two orthogonally linearly-polarized 118-GHz receivers, labeled R1A and R1B. R1A couples to radiation with magnetic field vector ($\hat{\boldsymbol{H}}$) nearly horizontal at the tangent point of the limb path while R1B couples to radiation with $\hat{\boldsymbol{H}}$ nearly vertical.

Our polarized radiative transfer model is based upon the work of Lenoir [4][5], who developed the theory of polarized radiative transfer using 2x2 coherence matrices, and applied this theory to Zeeman-split microwave oxygen lines. Further relevant work has been done by Rosenkranz and Staelin [6] and Stogryn [7].

II. Spectroscopy

The electronic ground state of diatomic oxygen (O_2) has a pair of aligned electronic spins (electronic spin quantum number $s = 1$) with an associated magnetic dipole moment. Oxygen's microwave spectrum consists of magnetic dipole transitions that reorient this spin relative to the molecule's end-over-end rotation (quantum number N). The 118-GHz oxygen line is a transition between two states that both have $N \approx 1$. (N is actually not a "good" quantum number, as the corresponding stationary states are not composed purely of spin-rotation basis states of a single N, but the predominant
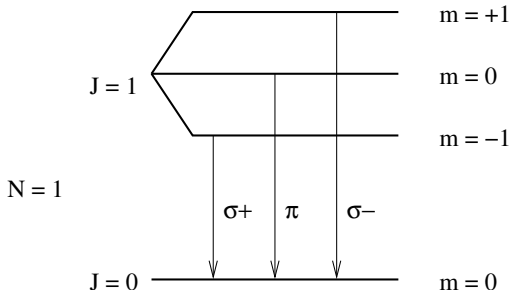
Fig. 1. The 1_- line has three Zeeman components. This figure is not to scale as all three transitions are approximately 118751 MHz, while the Zeeman splitting in typical geomagnetic fields is only of order 1 MHz.

Fig. 2. Angles θ and ϕ define the orientation or the geomagnetic field $\mathcal{B}_{geo}$ relative to the x and y linear polarization basis for a wave propagating in the z direction.

value of N is a useful label.) The upper state has three possible projections (quantum number m) of J on the direction of an external magnetic field, and the associated time-averaged projection of μ on the external field results in Zeeman splitting of the line, as shown schematically in Fig. 1. Lines of this type are labeled $N_{\Delta m}$; the 118-GHz line is 1_-. The energy shift due to the magnetic splitting is $mg\mu_B\mathcal{B}_{geo}$, where $\mathcal{B}_{geo}$ is the magnitude of the geomagnetic field, μ_B is the Bohr magneton, and the line-dependent constant, g, is given in the JPL spectral line database [8]. For the upper state of the 1_- line, $g = 1.0011$, the same value that one obtains from a simple, Hund's case b vector model [9]. The shifts of the m=±1 states from the m=0 state for $J = 1$ are ±140.12 MHz per μT of applied field, or less than ±1 MHz in typical geomagnetic fields.

III. TENSOR MAGNETIC SUSCEPTIBILITY

Under the influence of an applied magnetic field (such as the geomagnetic field), oxygen has a 3x3, rank-2 tensor magnetic susceptibility, $\chi^{(3)}$, which couples different components of the magnetic fields H and B through the constitutive relation [10][11]

$$B = \mu_0(1 + \chi^{(3)})H. \quad (1)$$

Magnetic dipole transitions change the magnetic quantum number, m, by +1, 0 or −1, and are labeled σ_+, π, and σ_-, respectively. The three eigenvectors of the tensor magnetic susceptibility, $\chi^{(3)}$, link three radiation polarizations to these three allowed values of Δm. The factoring of a common angular dependence for all lines in each of σ_+, π, and σ_- is a manifestation of the Wigner-Eckart theorem [4].

Linearly-polarized radiation with its H vector along the imposed field direction couples only to π transitions while right and left-circular polarizations propagating along the external field couple only to σ_+ and σ_- transitions, respectively. Knowing these eigen polarizations, we can write the angular dependence of $\chi^{(3)}$ in a right-hand, Cartesian basis where the third dimension is the direction of the externally applied field.

$$\chi^{(3)} = \begin{bmatrix} (\chi_+ + \chi_-)/2 & -\imath(\chi_+ - \chi_-)/2 & 0 \\ \imath(\chi_+ - \chi_-)/2 & (\chi_+ + \chi_-)/2 & 0 \\ 0 & 0 & \chi_0 \end{bmatrix}. \quad (2)$$

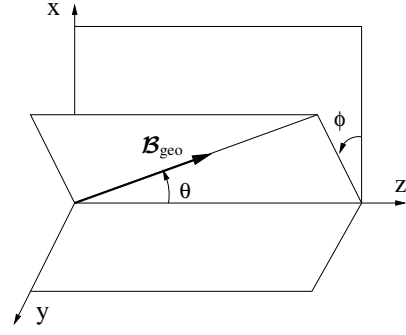Here, χ_+, χ_- and χ_0 are the eigenvalues of $\chi^{(3)}$.

Now we rotate $\chi^{(3)}$ (a rank-2 tensor rotates with a pair of 3x3 rotation matrices) so that $\hat{z}$ is the direction of propagation of a plane wave and $\hat{x}$ and $\hat{y}$ are a linear transverse polarization basis. The polarization direction is defined to be that of the radiation E-field. The rotation angles, θ and ϕ, are defined in Fig. 2.

If the magnetic-dipole coupling is weak ($\chi_{ij} \ll 1$), as is the case for the transitions considered here, waves propagating through the medium are approximately transverse [4] and the $\hat{z}$ dimension may be dropped from the radiation field equations. As $\hat{H}$ is confined to the $x - y$ plane, there is no need for z-components of $\chi^{(3)}$ and we project it into the two transverse dimensions.

$$\chi = \chi_+\rho_+ + \chi_0\rho_0 + \chi_-\rho_-, \quad (3)$$

where

$$\rho_\pm = R_\phi \begin{bmatrix} 1 & \mp\imath\cos\theta \\ \pm\imath\cos\theta & \cos^2\theta \end{bmatrix} R_\phi^\dagger, \quad (4)$$

$$\rho_0 = R_\phi \begin{bmatrix} 0 & 0 \\ 0 & \sin^2\theta \end{bmatrix} R_\phi^\dagger, \quad (5)$$

and

$$R_\phi = \begin{bmatrix} \cos\phi & \sin\phi \\ -\sin\phi & \cos\phi \end{bmatrix}. \quad (6)$$

Here, † denotes Hermitian adjoint, which is the complex conjugate transpose. The coefficients χ_+, χ_- and χ_0 are complex scalars, sums of the lineshapes of all lines of a given Δm, while the ρ matrices couple the polarization modes.

IV. POLARIZED RADIATIVE TRANSFER

Polarized radiative transfer expressions govern the evolution of the intensity matrix, I, as radiation propagates through the atmosphere. We use the form of I from Lenoir [4]:

$$I = \begin{bmatrix} I_\parallel & I_| + \imath I_\circ \\ I_| - \imath I_\circ & I_\perp \end{bmatrix}, \quad (7)$$

where $I_\parallel$ and $I_\perp$ are radiated power in linear polarizations respectively parallel and perpendicular to a reference direction, in our case the direction of linear polarization of an MLS receiver. $I_\circ$ and $I_|$ are the circular and linear coherences of the polarizations.

TABLE I
SYMBOL TABLE

$\hat{\boldsymbol{H}}, \hat{\boldsymbol{E}}$	Magnetic and Electric field unit vectors defining a linear radiation mode.
$\boldsymbol{\mathcal{B}}_{\text{geo}}$	Geomagnetic Field.
$\boldsymbol{\chi^{(3)}}$	3x3 tensor magnetic susceptibility.
$\boldsymbol{\chi}$	2x2 Hermitian matrix projection of $\boldsymbol{\chi^{(3)}}$ into the transverse plane.
J, m	Total molecular angular momentum and its projection along applied magnetic field.
σ_+, π, σ_-	Label transitions where $\Delta m = +1$, 0, -1 respectively.
$\boldsymbol{\rho}_+, \boldsymbol{\rho}_0, \boldsymbol{\rho}_-$	2x2 bases for $\boldsymbol{\chi}$.
$\boldsymbol{I}$	2x2 Intensity matrix.
$\boldsymbol{\mathcal{T}}_i$	2x2 power transmittance matrix from the ith layer boundary to the observer. $\boldsymbol{\mathcal{T}}_i = \boldsymbol{P}_i \boldsymbol{P}_i^\dagger$
$\boldsymbol{P}_i$	2x2 field transmittance matrix from the ith layer boundary to the observer. $\boldsymbol{P}_i = \boldsymbol{P}_{i-1} \boldsymbol{E}_i$
$\boldsymbol{E}_i$	2x2 field transmittance matrix from layer boundary $i \to i-1$. $\boldsymbol{E}_i = \exp - \sum_k^{\text{species}} \boldsymbol{\Delta\delta}_{i\to i-1}^k$
ΔB_i	Scalar differential temperature.
$\boldsymbol{\Delta\delta}_{i\to i-1}^k$	2x2 field incremental opacity for species k.
$\beta_{\Delta m}^k$	cross-section for species, k.
ζ	$-\log_{10}(\text{Pressure}/1\,\text{hPa})$. Vertical coordinate for representation of the atmosphere.
ϕ	horizontal coordinate for representation of the atmosphere (a latitude-like angle in the sub-orbital plane.)
η_l^T, η_m^T	triangular vertical and horizontal representation basis elements, used to formally make a continuous, linearly interpolated representation of the atmosphere from a set of discrete coefficients. [12].
$\mathcal{F}$	Complex lineshape function.
$\boldsymbol{G}(\Omega - \Omega_t)$	Antenna pattern as a function of solid-angle displacement from pattern center.
ν	The discrete frequency at which radiative transfer calculations are performed.
$\mathcal{M}^k$	Molecular mass of absorber species k.

We adopt the limb-path layer indexing scheme of the unpolarized algorithm [1], in which the first layer boundary is the top of the atmosphere closest to the observer, the tangent point is doubly-labeled t and $2N - t + 1$, and the top of the atmosphere beyond the tangent point is $2N$. This indexing is shown in Fig. 3. Double-indexing of the tangent point facilitates insertion of a surface term when rays intersect the earth's surface.

An expression for polarized radiation emerging from the top of the atmosphere along a limb path may be cast in a differential-temperature form identical to that used in the unpolarized model [1],

$$I = \sum_{i=1}^{t} \boldsymbol{\mathcal{T}}_i \Delta B_i + \sum_{i=2N-t+1}^{2N} \boldsymbol{\mathcal{T}}_i \Delta B_i . \quad (8)$$

The differential temperature, ΔB_i, is a function of B_i, the Planck source function at layer-boundary temperature, T_i,

$$B_i = \frac{h\nu}{k(\exp\{\frac{h\nu}{kT_i}\} - 1)} . \quad (9)$$

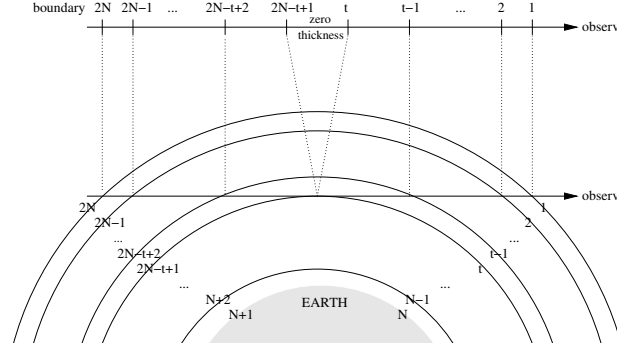$$\Delta B_i = \frac{B_{i+1} - B_{i-1}}{2} ,$$

Fig. 3. This indexing scheme labels layer boundaries along a limb path.

with special cases

$$\Delta B_1 = \frac{B_1 + B_2}{2} ,$$

$$\Delta B_{2N} = B(T_{cosmic}) - \frac{B_{2N} + B_{2N-1}}{2} ,$$

and, to handle the discontinuous indexing at the tangent point,

$$\Delta B_t = \frac{B_t - B_{t-1}}{2} ,$$

$$\Delta B_{2N-t+1} = \frac{B_{2N-t+2} - B_t}{2} . \quad (10)$$

The special cases are boundary terms from the transformation from a "differential absorption" form of the equations of radiative transfer to a "differential temperature" form. Gathering terms with common $\boldsymbol{\mathcal{T}}_i$ simplifies derivative expressions in Section VI. Radiances are in kelvin, so the leading factor in (9) is $h\nu/k$ rather than $2h\nu^3/c^2$.

$\boldsymbol{\mathcal{T}}_i$ is the *power* transmittance tensor from the ith layer boundary to the top of the atmosphere. It is the product of a pair of *field* transmittances, $\boldsymbol{P}_i$,

$$\boldsymbol{\mathcal{T}}_i = \boldsymbol{P}_i \boldsymbol{P}_i^\dagger . \quad (11)$$

$\boldsymbol{P}_i$ is constructed of *field* layer transmittances, $\boldsymbol{E}_i$, using the recursion relation,

$$\boldsymbol{P}_1 = \boldsymbol{1} ,$$
$$\boldsymbol{P}_i = \boldsymbol{P}_{i-1} \boldsymbol{E}_i ,$$

with a special case for the transmittance between the two instances of the tangent point,

$$\boldsymbol{P}_{2N-t+1} = \boldsymbol{P}_t \Upsilon_f . \quad (12)$$

For rays that intersect the geoid, Υ_f is the *field* surface reflectivity matrix, the square root of the *power* surface reflectivity, Υ, of [1]. Otherwise, Υ_f is unity. *Field* layer transmittances $\boldsymbol{E_i}$ are defined in terms of *field* incremental opacities, $\boldsymbol{\Delta\delta}_{i\to i-1}^k$

$$\boldsymbol{E}_1 = \boldsymbol{1} ,$$

$$\boldsymbol{E}_i = \exp\left[- \sum_k^{\text{species}} \boldsymbol{\Delta\delta}_{i\to i-1}^k\right] . \quad (13)$$

TABLE II
ZEEMAN FRACTIONAL INTENSITIES, $\xi(m, \Delta m)$

	Δm	N_+	N_-	1_-
σ_+	+1	$\frac{3(N+m+1)(N+m+2)}{4(N+1)(2N+1)(2N+3)}$	$\frac{3(N-m)(N-m-1)}{4N(2N+1)(2N-1)}$	$\frac{1}{2}$
π	0	$\frac{3[(N+1)^2-m^2]}{(N+1)(2N+1)(2N+3)}$	$\frac{3(N^2-m^2)}{N(2n+1)(2N-1)}$	1
σ_-	-1	$\frac{3(N-m+1)(N-m+2)}{4(N+1)(2N+1)(2N+3)}$	$\frac{3(N+m)(N+m-1)}{4N(2N+1)(2N-1)}$	$\frac{1}{2}$

Summation over species, k, explicitly allows contribution for absorbers other than oxygen. Matrix exponentiation is discussed in the appendix.

$\boldsymbol{\mathcal{T}}_i$ is manifestly Hermitian, composed of matrix pairs $\boldsymbol{E}_i$ and $\boldsymbol{E}_i^\dagger$ built up from the center outward, with the earliest times (largest indices) in the middle. Neglecting the discontinuity of indices at the tangent point,

$$\boldsymbol{\mathcal{T}}_i = \boldsymbol{E}_1 \boldsymbol{E}_2 \ldots \boldsymbol{E}_i \boldsymbol{E}_i^\dagger \ldots \boldsymbol{E}_2^\dagger \boldsymbol{E}_1^\dagger. \tag{14}$$

Order is important as the $\boldsymbol{E}_i$ matrices generally do not commute with one another.

The incremental opacity integral of the polarized O_2 lines is

$$\boldsymbol{\Delta\delta}_{i\to i-1}^{O_2} = \int_{s_i}^{s_{i-1}} \frac{\imath\pi\nu}{c} \boldsymbol{\chi} \, ds \tag{15}$$

$$= \frac{\Delta s_{i\to i-1}^{\text{refr}}}{\Delta s_{i\to i-1}} \sum_{\Delta m=-1}^{+1} \boldsymbol{\rho}_{\Delta m}(\theta,\phi) \, \xi_{m,\Delta m}$$

$$\times \int_{\zeta_i}^{\zeta_{i-1}} f^{O_2}(\zeta) \, \beta_{\Delta m}^{O_2}(\zeta), \nu) \frac{ds}{dh} \frac{dh}{d\zeta} \, d\zeta \, ,$$

where $\frac{\Delta s_{i\to i-1}^{\text{refr}}}{\Delta s_{i\to i-1}}$ is a correction for diffraction, as discussed in [12], fractional intensity, $\xi_{m,\Delta m}$ is from Table II, ν is frequency, c is the speed of light, and $f^{O_2}(\zeta)$ is the O_2 mixing ratio profile, and β is cross-section, discussed below in IV-A. The chain-rule for differentiation is used to transform from path-length s to height h to negative-log-pressure, ζ, which is used as the vertical coordinate in MLS retrievals. Expressions for $\frac{ds}{dh}$ and $\frac{dh}{d\zeta}$ are as in [1] or [12].

As is discussed in Section III, the $\boldsymbol{\rho}$ terms are functions only of the orientation of the propagation direction with respect to the geomagnetic field. They contain all of the angular dependence and all of the 2x2 tensor-nature of (15). These terms are common for all lines with the same Δm, though in the case of the 118-GHz line, there is only one Zeeman component for each Δm. All of the other terms in (15) are scalars.

For species that are isotropic absorbers, (i.e. $k \neq O_2$), the field incremental opacity matrix is half of the scalar power incremental opacity of [1] times the identity matrix.

$$\boldsymbol{\Delta\delta}_{i\to i-1}^k = \frac{1}{2}\Delta\delta_{i\to i-1}^k \, \boldsymbol{1} \, . \tag{16}$$

Polarized power transmittance, $\boldsymbol{\mathcal{T}}$, is formed from products of pairs of *field* transmittances, which depend exponentially upon the cross-sections. The two half-power cross-sections add so that each of the diagonal elements correctly gives the scalar result for unpolarized radiation. We can neglect the imaginary (dispersive) part of the incremental opacities for isotropic absorbers since $\boldsymbol{\Delta\delta}_{i\to i-1}^k$ is then proportional to the identity matrix, and it will commute through and cancel with its complex-conjugate pair in the construction of $\boldsymbol{\mathcal{T}}$.

A. Cross-Section $\boldsymbol{\beta}$

For oxygen Zeeman components, *field* cross-sections, β, have the same form as the *power* cross-sections of the scalar model, but in addition to the factor of one half, they require complex lineshapes, and Zeeman-shifts of the line center positions. Following the notation of [1], the field cross-section β^k is

$$\beta^k = \frac{1}{2} \, \mathcal{R}^k \, \sqrt{\frac{\ln 2}{\pi}} \frac{10^{-13}}{kT w_d^k} \, P \sum_j 10^{\mathcal{S}_j^k} \mathcal{F}\left(x_j^k, y_j^k\right) , \tag{17}$$

where $\mathcal{S}_j$ is the logarithm of line strength given in [12], and
- the index k is the species label ($k=O_2$)
- the subscript j identifies the individual lines of the molecule.
- $\mathcal{F}$ is the complex lineshape function,
- $\mathcal{R}^k$ is the isotopic fraction,
- T is temperature in Kelvins,
- P is pressure in hPa,
- $w_d = 3.58117369 \times 10^{-7}\nu\sqrt{\frac{T}{\mathcal{M}}}$ is the Doppler width,
- $\mathcal{M}$ is the absorber molecular mass.

B. Lineshape

The lineshape that we use for each of the Zeeman components is the Fadeeva function, or complex error function, [13] modified to include line interference. The Fadeeva function is the convolution of a Gaussian thermal Doppler lineshape with a Lorentzian collisional lineshape [14]. It has a simple form,

$$F(z) = \frac{\imath}{\pi} \int_{-\infty}^\infty \frac{e^{-t^2}}{z-t} \, dt$$

for complex z, or

$$F(x+\imath y) = \frac{1}{\pi} \int_{-\infty}^\infty e^{-t^2} \left(\frac{y}{(x-t)^2 + y^2} \right.$$
$$\left. + \frac{\imath(x-t)}{(x-t)^2 + y^2} \right) \, dt$$
$$= \mathcal{U}(x,y) + \imath\mathcal{V}(x,y) \, . \tag{18}$$

The real part of the Fadeeva function, $\mathcal{U}(x,y)$, is the Voigt function.

The first-order effect of interference with the lines of the 60-GHz O_2 band [15] is modeled by adding terms involving line mixing coefficients, Y_j. The contribution of these terms is negligible for the pressures where Zeeman-splitting is resolved, but they are included so that this model will merge smoothly with the unpolarized model at high pressures. The same mixing coefficient that is tabulated for the unpolarized case [1] is used for each Zeeman component.

Line interference can occur only between Zeeman components of the same Δm, so there is no interference among the Zeeman components of the 118-GHz oxygen line.

Rosenkranz [16] argues that this must be the case because interference between two transitions must be reciprocal in the sense that it acts oppositely on them. Isolation of one transition would imply a non-physical line shape (*e.g.* negative absorption). Zeeman components cannot be coupled if their relative strengths change with observation geometry, thus a component can only be coupled to another of the same Δm. This result can also be reached formally, starting from the impact approximation [17].

The expression that we use for the lineshape, including interference, is

$$\mathcal{F}(x_j, y_j) = \frac{1}{\pi} \frac{\nu}{\nu_{0j}} \int_{-\infty}^{\infty} e^{-t^2} \left(\frac{y_j - Y_j(x_j - t)}{(x_j - t)^2 + y_j^2} \right. \tag{19}$$
$$\left. + \frac{\imath(y_j Y_j + x_j - t)}{(x_j - t)^2 + y_j^2} \right) dt$$
$$= \frac{\nu}{\nu_{0j}} (1 + \imath Y_j) \mathcal{F}(x_j + \imath y_j), \tag{20}$$

where

$$x_j = \frac{\sqrt{\ln 2}\left(\nu - \nu_j^k - \Delta\nu_{j,m,\Delta m}\right)}{w_d^k},$$
$$y_j = \frac{\sqrt{\ln 2}\, w_{cj} P}{w_d^k} \left(\frac{T_0}{T}\right)^{n_{cj}^k},$$
$$Y_j = P \left[\delta_j^k \left(\frac{T_0}{T}\right)^{n_{\delta_j}^k} + \gamma_j^k \left(\frac{T_0}{T}\right)^{n_{\gamma_j}^k} \right],$$
$$w_d^k = \sqrt{2\ln 2\, \mathrm{k_B}/c} \sqrt{\frac{T}{\mathcal{M}^k}}\, \nu,$$

and the shifted line-center frequency is

$$\nu_j^k = \left[\nu_{0j}^k + \Delta\nu_{0j}^k P \left(\frac{T_0}{T}\right)^{n_{\Delta\nu_{0j}}^k}\right] \left(1 + \frac{v_{\mathrm{los}}}{c}\right). \tag{21}$$

Line parameters are tabulated in the MLS scalar forward model algorithm description [12]; these include unshifted line center frequency, ν_{0j}, collisional line width parameter, w_{cj}^k, collisional line width temperature dependence exponent, n_{cj}^k, line pressure shift parameter, $\Delta\nu_{0j}^k$ line pressure shift temperature dependence exponent, $n_{\Delta\nu_{0j}}^k$ and line interference parameters, δ_j^k, $n_{\delta_j}^k$, γ_j^k, $n_{\gamma_j}^k$. A line pressure shift, $\Delta\nu_{0j}^k$, has been included in the model, but has been set to zero based upon recent measurements that indicate a line-shift magnitude of less than 0.1 MHz/hPa [18][19].

The line-of-sight velocity, v_{los}, due to spacecraft motion, Earth rotation, and wind results in a Doppler shift that may be considered constant across the narrow spectral bandwidth of interest here.

The Zeeman frequency shifts are

$$\Delta\nu_{J,m,\Delta m} = (m_u/J_u g_u - m_l/J_l g_l)\mathcal{B}_{\mathrm{geo}}, \tag{22}$$

where g values for the upper and lower states are taken from the JPL catalog. [8] For the 118-GHz line, $J_u = 1$, $J_l = 0$

(recall Fig. 1) and the shifts are

$$\Delta\nu_{\sigma+} = \kappa\mathcal{B}_{\mathrm{geo}} \tag{23}$$
$$\Delta\nu_{\sigma-} = -\kappa\mathcal{B}_{\mathrm{geo}}$$
$$\Delta\nu_{\pi} = 0$$

where κ=14.012 kHz/μT.

The leading $\frac{\nu}{\nu_{0j}}$ in (19), which gives agreement with the Debye non-resonant shape at low frequencies, is nearly constant over the Doppler width, and taking it outside of the integral introduces negligible error.

The cross section is summed over all of the lines that contribute significantly. The z_j dependence of the lineshape in the MLS scalar forward model [12] explicitly includes the absorptive part of the negative-frequency resonance of each line. These terms give the absorption due to the far wing of the emission line at $-\nu_{0j}$, but are neglected here.

V. GEOMAGNETIC FIELD MODEL

We use geomagnetic field, $\mathcal{B}_{\mathrm{geo}}$, from the International Geomagnetic Reference Field (IGRF) model [20][21], an empirical representation of the Earth's core field. In the absence of magnetic storms, outside of the auroral belts, and below 120 km altitude, we estimate that IGRF represents the true geomagnetic field (including external sources) to 95 percent accuracy, but there is significant uncertainty in this value. Profiles of IGRF in the Earth centered rotating (ECR) frame are included in the Level 2 state vector. (Level-1 algorithms produce calibrated radiances. Level 2 algorithms retrieve atmospheric constituents from these radiances.) They are interpolated, as needed, to positions along the integration path and rotated to the instrument field of view polarized pointing (IFOVPP) coordinate system. The IFOVPP is defined by the linear polarization of the antenna, with received radiation propagating in the $\hat{z}$ direction, with its electric field in the $\hat{x}$ direction. and its magnetic field in the $\hat{y}$ direction. The linear polarizations of the two MLS 118-GHz receivers (R1A, R1B) are orthogonal to better than our $0.5°$ measurement precision [22], so calculated R1B radiances on the pointing grid (before frequency and pointing convolution) are taken to be the cross-polarization of the R1A calculation. Rotation matrices from the Earth-centered-rotating (ECR) frame (on which IGRF is defined) to the IFOVPP frame are provided for each 1/6-second MLS "minor-frame" integration (MIF), for the polarization and pointing of the central axis of the R1A antenna at the middle of each integration. These matrices are required to transform geomagnetic field into the frame in which radiative transfer calculations are performed. The radiative transfer calculations are done on a grid of pointing angles which is subsequently convolved with the antenna pattern [22] to give MIF-modeled radiances. The ECR-to-IFOVPP transformation is required, not for the MIF pointings, but on the radiative-transfer pointing grid. We use the rotation matrix from the closest MIF. Pointings in the radiative transfer grid that have higher tangent points than that of the highest tangent-point MIF all use the rotation matrix for the highest MIF. Errors introduced are small compared to those from other sources of uncertainty in the magnetic field.

VI. Derivatives

A. General Form of Polarized Derivatives

The equation of polarized radiative transfer, (8), may be differentiated with respect to a state vector element, x, to give the derivatives required by retrievals [3]. Care must be taken in the tensor case to preserve matrix order. In the following expressions, we do not explicitly show the break in indexing at the tangent point.

$$
\begin{aligned}
\frac{\partial \boldsymbol{I}(x)}{\partial x} &= \frac{\partial}{\partial x} \sum_{i=1}^{2N} \boldsymbol{\mathcal{T}}_i \, \Delta B_i \\
&= \sum_{i=1}^{2N} \frac{\partial \boldsymbol{\mathcal{T}}_i}{\partial x} \Delta B_i + \boldsymbol{\mathcal{T}}_i \frac{\partial \Delta B_i}{\partial x}
\end{aligned} \quad (24)
$$

The derivative of $\boldsymbol{\mathcal{T}}_i$ may be built up, for successive layers, by differentiating the recurrence relation, $\boldsymbol{P}_i = \boldsymbol{P}_{i-1}\boldsymbol{E}_{i-1}$.

$$
\frac{\partial \boldsymbol{P}_i}{\partial x} = \frac{\partial \boldsymbol{P}_{i-1}}{\partial x}\boldsymbol{E}_{i-1} + \boldsymbol{P}_{i-1}\frac{\partial \boldsymbol{E}_{i-1}}{\partial x} \quad (25)
$$

with

$$
\frac{\partial \boldsymbol{\mathcal{T}}_i}{\partial x} = \frac{\partial \boldsymbol{P}_i}{\partial x}\boldsymbol{P}_i^{\dagger} + \left(\frac{\partial \boldsymbol{P}_i}{\partial x}\boldsymbol{P}_i^{\dagger}\right)^{\dagger}. \quad (26)
$$

The differentiation of a matrix exponential is discussed in the appendix.

B. Mixing Ratio Derivatives

Mixing ratio coefficients are f_{lmn}^k where k refers to the species, l is vertical coordinate (ζ), m is horizontal coordinate (ϕ) and n is frequency (ν). Frequency is included for the case of EXTINCTION (see [1]), which may be treated as a frequency-dependent species. The expression for incremental opacity (15) is a sum of terms linear in mixing ratio, so these derivatives are simply expressed by dropping f^k and the summation over species k.

$$
\begin{aligned}
\frac{\partial \boldsymbol{\Delta}\delta_{i\to i-1}^k}{\partial f_{lmn}^T} &= \sum_{\Delta m=-1}^{+1} \boldsymbol{\rho}_{\Delta M}(\theta,\phi) \\
&\times \int_{\zeta_i}^{\zeta_{i-1}} \beta_{\Delta m}^k(\zeta,\nu,T,\boldsymbol{\mathcal{B}}_{\text{geo}}) \frac{\mathrm{d}s}{\mathrm{d}h}\frac{\mathrm{d}h}{\mathrm{d}\zeta}\,\mathrm{d}\zeta. \quad (27)
\end{aligned}
$$

The term in (24) involving $\frac{\partial \Delta B_k}{\partial x}$ is zero for mixing ratio derivatives because ΔB_k depends only upon temperature.

The volume mixing ratio (VMR) of $^{16}O_2$ is not retrieved from the MLS data. In the thermosphere, where O_2 VMR begins to drop significantly, O_2 lines are Doppler broadened and there is not enough information to separate temperature from mixing ratio. We currently use the same a priori O_2 profile as was used with UARS MLS, which is piecewise-linear in $\zeta \equiv -\log_{10}(P/1\,\mathrm{hPa})$. The break-points of this profile are given in Table III.

ζ	O_2 VMR	approx. height
surface	0.2095	0 km
2.10	0.2095	82 km
2.78	0.2080	91 km
3.52	0.2032	100 km
4.18	0.1447	110 km

C. Temperature Derivatives

Temperature derivatives are complicated because atmospheric absorption and emission, the source function and the path length (through the hydrostatic model) all depend upon temperature. Fortunately, most of this complexity is identical to that of the unpolarized case. In the polarized expressions, β for each Δm multiplies an appropriate tensor, $\boldsymbol{\rho}$, and is summed over Δm. As in [1], the temperature state is represented as the linear interpolation of a set of coefficients on a grid. It is with respect to these coefficients, f_{lm}^T, where l is vertical coordinate (ζ) and m is horizontal coordinate (ϕ), that we wish to differentiate.

As in the unpolarized case, a simplified incremental opacity is used that neglects the temperature dependence in refraction and uses a simplified $\frac{dh}{d\zeta}$. The frequency representation basis is dropped since temperature has no frequency dependence. The simplified incremental opacity has the form

$$
\begin{aligned}
\Delta\delta_{i\to i-1}^k =& \frac{\Delta s_{i\to i-1}^{\text{refr}}}{\Delta s_{i\to i-1}} \sum_{\Delta m=-1}^{+1} \boldsymbol{\rho}_{\Delta m}(\theta,\phi) \\
&\times \int_{\zeta_i}^{\zeta_{i-1}} \mathsf{f}^k(\zeta,\phi(\zeta),\nu)\,\beta_{j,\Delta m}^k(\zeta,\nu,T,\boldsymbol{\mathcal{B}}_{\text{geo}}) \\
&\times \frac{H^3}{\sqrt{H^2-H_t^2}}\frac{Tk\ln 10}{g_o R_o^2 \mathcal{M}}\,\mathrm{d}\zeta. \quad (28)
\end{aligned}
$$

Here, H_t and H are the distance from the "equivalent circular" Earth center to the tangent point and to a point along the tangent path, as discussed in [1] and [12].

Differentiating with respect to temperature gives

$$
\begin{aligned}
\frac{\mathrm{d}\Delta\delta_{i\to i-1}^k}{\mathrm{d}f_{lm}^T} =& \frac{\Delta s_{i\to i-1}^{\text{refr}}}{\Delta s_{i\to i-1}} \sum_{\Delta m=-1}^{+1} \boldsymbol{\rho}_{\Delta m}(\theta,\phi) \\
&\times \int_{\zeta_i}^{\zeta_{i-1}} \Bigg\{ \mathsf{f}^k \frac{\mathrm{d}\beta_{j,\Delta m}^k(\zeta)}{\mathrm{d}f_{lm}^T}\,\eta_l^T(\zeta)\,\eta_m^T(\phi(\zeta))\frac{\mathrm{d}s}{\mathrm{d}h}\frac{\mathrm{d}h}{\mathrm{d}\zeta} \\
&+ \mathsf{f}^k\beta_{j,\Delta m}^k(\zeta)\frac{2H^2\frac{\mathrm{d}H}{\mathrm{d}f_{lm}^T}-3H_t^2\frac{\mathrm{d}H}{\mathrm{d}f_{lm}^T}+HH_t\frac{\mathrm{d}H_t}{\mathrm{d}f_{lm}^T}}{(H^2-H_t^2)^{\frac{3}{2}}}\frac{\mathrm{d}h}{\mathrm{d}\zeta} \\
&+ \mathsf{f}^k\beta_{j,\Delta m}^k(\zeta)\frac{\eta_l^T(\zeta)\,\eta_m^T(\phi(\zeta))}{T}\frac{\mathrm{d}s}{\mathrm{d}h}\frac{\mathrm{d}h}{\mathrm{d}\zeta}\Bigg\}\mathrm{d}\zeta.
\end{aligned}
$$
$$(29)$$

Apart from the summation over Δm and the $\boldsymbol{\rho}$ matrices, this expression is identical to the unpolarized case [1] except that here we have both the real and imaginary parts of the lineshape in the temperature derivative of β. The derivative of

the lineshape, (19), is

$$\frac{\mathrm{d}F(x_j, y_j)}{\mathrm{d}T} = \frac{\nu}{\nu_{0j}} \left[(1 + \imath Y_j) \frac{\mathrm{d}\mathcal{U}}{\mathrm{d}x} \frac{\mathrm{d}x}{\mathrm{d}T} \right.$$
$$+ (1 + \imath Y_j) \frac{\mathrm{d}\mathcal{U}}{\mathrm{d}y} \frac{\mathrm{d}y}{\mathrm{d}T}$$
$$+ \imath \frac{\mathrm{d}Y}{\mathrm{d}T} \mathcal{U} + \imath (1 + \imath Y_j) \frac{\mathrm{d}\mathcal{V}}{\mathrm{d}x} \frac{\mathrm{d}x}{\mathrm{d}T}$$
$$\left. + \imath (1 + \imath Y_j) \frac{\mathrm{d}\mathcal{V}}{\mathrm{d}y} \frac{\mathrm{d}y}{\mathrm{d}T} - \frac{\mathrm{d}Y}{\mathrm{d}T} \mathcal{V} \right]. \quad (30)$$

The derivatives of the real and imaginary parts of the Fadeeva function are

$$\frac{\partial \mathcal{U}}{\partial y} = \frac{\partial \mathcal{V}}{\partial x} = 2y\mathcal{V} - 2x\mathcal{U},$$
$$\frac{\partial \mathcal{U}}{\partial x} = -\frac{\partial \mathcal{V}}{\partial y} = 2y\mathcal{V} + 2x\mathcal{U} - 2/\sqrt{\pi}. \quad (31)$$

Expressions for $\frac{\mathrm{d}\nu_j^k}{\mathrm{d}T}$, $\frac{\mathrm{d}x_j^k}{\mathrm{d}T}$, $\frac{\mathrm{d}y_j^k}{\mathrm{d}T}$, and $\frac{\mathrm{d}Y_j^k}{\mathrm{d}T}$ may be found in [12, Equation 9.8].

D. $\boldsymbol{\beta}$ Derivatives

Derivatives of quantities on which $\Delta\delta_{i+1\to i}^k$ has dependence only through β can be written

$$\frac{\partial \boldsymbol{\Delta\delta}_{i\to i-1}^k}{\partial x_j} = \sum_{\Delta m=-1}^{+1} \boldsymbol{\rho}_{\Delta M} \int_{\zeta_i}^{\zeta_{i-1}} f_{lmn}^k \frac{\mathrm{d}\beta_{\Delta m}^k}{\mathrm{d}x_j} \frac{\mathrm{d}s}{\mathrm{d}h} \frac{\mathrm{d}h}{\mathrm{d}\zeta} \, \mathrm{d}\zeta \,. \tag{32}$$

This class includes derivatives with respect to spectroscopic parameters, wind-induced Doppler shifts, and magnetic field.

VII. FIELD OF VIEW CONVOLUTION

The method of field-of-view convolution is discussed in [1] and [12].

$$I(\Omega_t) = \frac{\mathrm{Tr} \int_{\Omega_A} \boldsymbol{I}(\Omega) \, \boldsymbol{G}(\Omega - \Omega_t) \, \mathrm{d}\Omega}{\mathrm{Tr} \int_{\Omega_A} \boldsymbol{G}(\Omega - \Omega_t) \, \mathrm{d}\Omega}, \tag{33}$$

where Ω is the solid angle over which radiative transfer has been calculated, Ω_t is the pointing of the antenna to be modeled and Ω_A is the solid angle over which the polarized, far-field antenna pattern tensor, $\boldsymbol{G}(\Omega - \Omega_t)$, has been measured. For both R1A and R1B, the cross-polarized antenna patterns are at least 30 dB less than the co-polarized patterns [22]. Currently, the cross-polarization is ignored, permitting the use of the same software as is used in the unpolarized case. Resulting errors in calculated brightness temperatures are estimated to be less than 0.2 K. After field-of-view convolution, power is a scalar so the unpolarized, scalar algorithm for frequency averaging [1] may be followed without approximation.

VIII. PRECOMPUTED DERIVATIVES

The MLS Level 2 retrieval software [3] requires Jacobians, partial derivatives of the radiances with respect to state vector elements. Unfortunately, the cost of producing polarized derivatives during routine processing is currently prohibitive, so radiances and derivatives are precomputed for a climatological temperature profile and tabulated as Level 2 processing coefficient (L2PC) files. In the first publicly-released MLS data version, v01.51, precomputed derivatives are used but the radiance calculation is iterated using the full, polarized forward model.

The polarized L2PC files contain temperature derivatives for MLS bands 22 and 26 (the DACS bands used for Zeeman-split O_2) for each point on a grid of magnetic field strengths and orientations. The closest grid points of field strength and elevation angle (the angle between the field and the line-of-sight) to the desired field values are used.

Interpolation in azimuth angle, ϕ, is done analytically. From (7) and (6) we obtain

$$I_\|(\phi) = \cos^2(\phi)I_\|(0°) + \sin^2(\phi)I_\perp(0°)$$
$$+ 2\cos(\phi)\sin(\phi)I_|(0°). \tag{34}$$

In its current configuration, the polarized L2PC model assumes a constant geomagnetic field magnitude and orientation along the integration path. This permits the model to be parameterized by the field value at the tangent point. However, the full forward model (and the real atmosphere) have geomagnetic field variations along the path with resulting radiances that cannot be modeled with a constant field. For example, variation in the field magnitude along the integration path will shift the $\sigma_\pm$ components in and out, resulting in a broadened spectral feature with weighting functions that depend upon the details of the field along the path. The impact of this approximation upon EOS-MLS retrievals is an area for further research.

IX. RESULTS FROM EARLY MLS DATA

Fig. 4 shows simulated, single-frequency, single-ray limb radiances for the 61 DACS channels that are used in MLS retrievals. Seven limb-pointings are shown, with tangent pressures ranging from 1000 hPa to 0.0001 hPa. The six panels are for six orientations of geomagnetic field, $\boldsymbol{\mathcal{B}}_{\mathrm{geo}}$, with inset axes showing the orientation of $\boldsymbol{\mathcal{B}}_{\mathrm{geo}}$ with respect to the propagation direction ($\hat{z}$) and with respect to $\hat{\boldsymbol{E}}$ and $\hat{\boldsymbol{H}}$, the directions of the $\boldsymbol{E}$ and $\boldsymbol{H}$ fields of the linearly-polarized radiation, respectively. In the top three panels from left to right, $\boldsymbol{\mathcal{B}}_{\mathrm{geo}}$ is in the $\hat{z}$, $\hat{\boldsymbol{E}}$ and $\hat{\boldsymbol{H}}$ directions, and figures are symmetric under a sign change of $\boldsymbol{\mathcal{B}}_{\mathrm{geo}}$. In the bottom three panels from left to right, $\boldsymbol{\mathcal{B}}_{\mathrm{geo}}$ is in the $\hat{z}$-$\hat{\boldsymbol{E}}$ plane, in the $\hat{z}$-$\hat{\boldsymbol{H}}$ plane and in the $\hat{\boldsymbol{H}}$-$\hat{\boldsymbol{E}}$ plane The geomagnetic field magnitude is 50 μT in all cases. Single-frequency, single-pointing simulated radiances such as these are convolved with MLS channel frequency response functions and antenna patterns to produce simulated channel radiances.

In the upper right panel, $\boldsymbol{\mathcal{B}}_{\mathrm{geo}}$ is along $\hat{\boldsymbol{H}}$ and the π line center is saturated at roughly the physical temperature of the lower thermosphere for the 0.001-hPa pointing. This is also what is seen for the unpolarized (zero field) case. The upper center panel, with $\boldsymbol{\mathcal{B}}_{\mathrm{geo}}$ perpendicular to both $\hat{\boldsymbol{H}}$ and the propagation direction, has two opaque σ lines all the way up to the 0.001-hPa pointing. In the upper left panel, the σ lines are coupled to circularly polarized modes (σ_+ is right, σ_- is left) and the π line is transparent. On the 0.001 hPa tangent pointing, a right-circularly-polarized receiver would

see only the $\sigma+$ line, and would be a shifted version of the upper right panel, saturated slightly below 200 K. The MLS linearly polarized receiver sees half of the saturated right-circular and half of the transparent left-circular modes at the $\sigma+$ line center, and appears to saturate for the 0.001-hPa pointing at roughly half of the physical temperature of the lower thermosphere. The atmosphere is not opaque along a tangent path for a linear polarization until pressure broadening makes both circular polarizations opaque at a give frequency, so the radiances do not fully saturate at the line centers until between the 0.032 hPa and 0.1 hPa tangent-pressure pointings.

Fig. 5 and Fig. 6 show comparisons of MLS measurements and the corresponding forward model calculations from an MLS Level-2 retrieval that uses these radiances. The placement and strengths of the lines is in good general agreement between the model and observation, but the highest-altitude observed line-center radiances are as much as 40 K higher than those of the forward model. This deficiency is consistent with an insufficiently steep retrieved temperature gradient into the thermosphere, and may be a deficiency of the retrieval configuration rather than of the forward model *per se*. At mid and high latitudes, R1A mostly sees the pair of σ lines while R1B sees a nearly-pure π line. The π line has the same integrated absorption of the two σ lines, so it is stronger and saturates higher in the thermosphere, making it more sensitive to the highest-altitude temperatures of the retrieved profile. The larger radiance residuals observed in the R1B line center are consistent with the highest-altitude temperature of the retrieval not being high enough. Initial attempts to address this problem have not been successful, but it is under investigation.

X. CONCLUSIONS AND FURTHER WORK

Radiative transfer in the vicinity of Zeeman-split lines is polarization-dependent, and polarization modes are coupled, requiring that calculations account for both modes and their relative phase. A model for radiances and their derivatives with respect to atmospheric parameters (retrieval state vector elements) has been implemented to account for Zeeman splitting of the 118-GHz oxygen line. EOS MLS has a pair of linearly cross-polarized radiometers with 100-kHz resolution spectrometers covering this line center. At the highest-tangent-altitude limb pointings of MLS, line center radiances change by more than 200 K with a change in polarization, and all O_2 line-center radiances are somewhat impacted by Zeeman splitting since the lower atmosphere must be viewed through opaque high-altitude line centers. MLS temperature retrievals are significantly impacted by polarization effects above 1 hPa.

The polarized forward model is used operationally by the MLS version 01.51 Level-2 software for the modeling of radiances near the 118-GHz oxygen line in the retrieval of mesospheric and lower-thermospheric temperature. Modeled and observed radiances have very similar dependence upon orientation of the geomagnetic field with respect to the radiation propagation and polarization directions.

Persistent high-altitude residuals in the line centers, particularly in R1B shown in Fig. 6, may be an indication that the current temperature retrieval does not have sufficient degrees of freedom at the highest altitudes. The adequacy of the Level-2 configuration is currently under investigation. Residuals may also result from the use of precomputed, climatological partial-derivatives of radiances with respect to temperature-profile elements. These derivatives assume that magnetic field is constant at its tangent-point value along the entire tangent path, which may cause problems far from the tangent point. Current computing resources necessitate the use of these climatological derivatives in routine processing, and their adequacy is under investigation.

APPENDIX

Expressions for matrix exponentials and their derivatives are needed for (13) and (25). The exponential of a 2x2 matrix (Sylvester's identity) is

$$\exp(\boldsymbol{A}) = e^{\lambda_2}\left[\frac{e^{2d}-1}{2d}(\boldsymbol{A}-\lambda_2\mathbf{1})+\mathbf{1}\right], \qquad (35)$$

where λ_1, λ_2 are eigenvalues of $\boldsymbol{A}$, $d \equiv \frac{1}{2}(\lambda_1 - \lambda_2)$ and $\mathbf{1}$ is the 2×2 identity matrix. This form is well behaved as $d \to 0$. The derivative of a matrix exponential with respect to p is

$$\frac{\mathrm{d}\exp(\mathbf{A})}{\mathrm{d}p} = e^s\left\{\frac{\sinh d}{d}\left[s'\mathbf{A}+\mathbf{A}'+(d'd-s's)\mathbf{I}\right]\right.$$
$$\left.+\frac{d\cosh d - \sinh d}{d^2}\left[d'\mathbf{A}+(s'd-d's)\mathbf{I})\right]\right\},$$
$$(36)$$

where $s \equiv \frac{1}{2}(\lambda_1+\lambda_2)$, $d' = \frac{\mathrm{d}d}{\mathrm{d}p}$, $s' = \frac{\mathrm{d}s}{\mathrm{d}p}$, $\boldsymbol{A}' = \frac{\mathrm{d}\boldsymbol{A}}{\mathrm{d}p}$. As the eigenvalues coalesce, no cancellations occur, and no infinities arise if the elements of $\mathbf{A}$ and $\mathbf{A}'$ are finite.

REFERENCES

[1] W. G. Read, Z. Shippony, M. J. Schwartz, N. J. Livesey, and W. V. Snyder, "The clear-sky unpolarized forward model for the EOS Aura microwave limb sounder (MLS)," *IEEE Trans. Geosci. Remote Sensing: The EOS Aura mission*, 2005, this issue.

[2] J. W. Waters *et al.*, "The earth observing system microwave limb sounder (EOS MLS) on the aura satellite," *IEEE Trans. Geosci. Remote Sensing: The EOS Aura mission*, 2005, this issue.

[3] N. J. Livesey, W. V. Snyder, W. G. Read, and P. A. Wagner, "Retrieval algorithms for the EOS Microwave Limb Sounder (MLS) instrument," *IEEE Trans. Geosci. Remote Sensing: The EOS Aura mission*, 2005, this issue.

[4] W. B. Lenoir, "Propagation of partially polarized waves in a slightly anisotropic medium," *Journal of Applied Physics*, vol. 38, no. 13, 1967.

[5] ——, "Microwave spectrum of molecular oxygen in the mesosphere," *Journal of Geophysical Research*, vol. 73, no. 361, 1968.

[6] P. W. Rosenkranz and D. H. Staelin, "Polarized thermal microwave emission from oxygen in the mesosphere," *Radio Science*, vol. 23, no. 5, pp. 721–729, September–October 1988.

[7] A. Stogryn, "The magnetic field dependence of brightness temperatures at frequencies near the O_2 microwave absorption lines," *IEEE Transactions on Geoscience and Remote Sensing*, vol. 27, no. 3, pp. 279–289, May 1989.

[8] H. M. Pickett, R. L. Poynter, E. A. Cohen, M. L. Delitsky, J. C. Pearson, and H. S. P. Muller, "Submillimeter, millimeter, and microwave spectral line catalog," *J. Quant. Spectrosc. Radiat. Transfer*, vol. 60, no. 5, pp. 883–890, 1998. [Online]. Available: see http://spec.jpl.nasa.gov/

[9] C. H. Townes and A. L. Schawlow, *Microwave Spectroscopy*. New York: Dover Publications, Inc., 1955.

[10] J. D. Jackson, *Classical Electrodynamics*, 2nd ed. Wiley, 1975.

[11] E. Weisstein. (2005, 22 February) Eric weisstein's world of physics. [Online]. Available: http://scienceworld.wolfram.com/physics/H.html
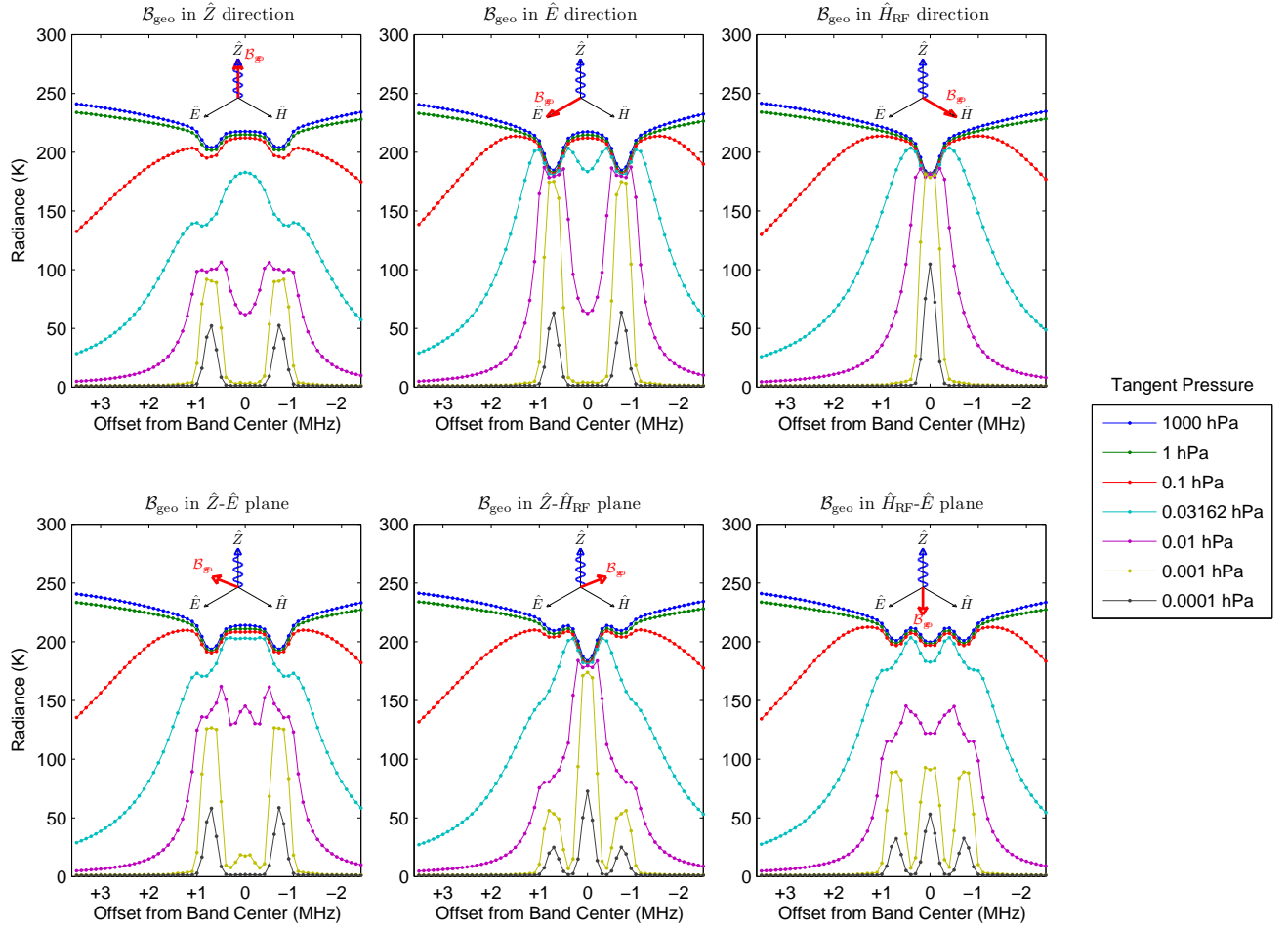
Fig. 4. Single-frequency, single-ray, calculated limb radiances for the Zeeman components of the 118-GHz O_2 line. The six panels show modeled radiances for six orientations of geomagnetic field, $\mathcal{B}_{\text{geo}}$, with respect to the polarization and propagation directions of the linear polarization mode under consideration. In all cases, geomagnetic field magnitude is 50 μT. Doppler-broadened cores of the lines are fully saturated at 0.001 hPa for some polarization, but not necessarily for that of the observation. In the top left panel, propagation is along $\mathcal{B}_{\text{geo}}$ and the σ_+ (higher frequency) and σ_- (lower frequency) lines are right and left circularly polarized respectively. Along the 0.001 hPa tangent-pressure ray, the line centers are opaque for one circular mode and transparent for the other and a linear polarization consists of half of each. In the top middle panel, $\mathcal{B}_{\text{geo}}$ is aligned with $\hat{E}$ and the $\sigma_\pm$ lines are linearly co-polarized with the mode under consideration. In the top right panel, $\mathcal{B}_{\text{geo}}$ is aligned with the antenna's $\hat{H}$ direction and the π line is co-polarized with the mode under consideration.
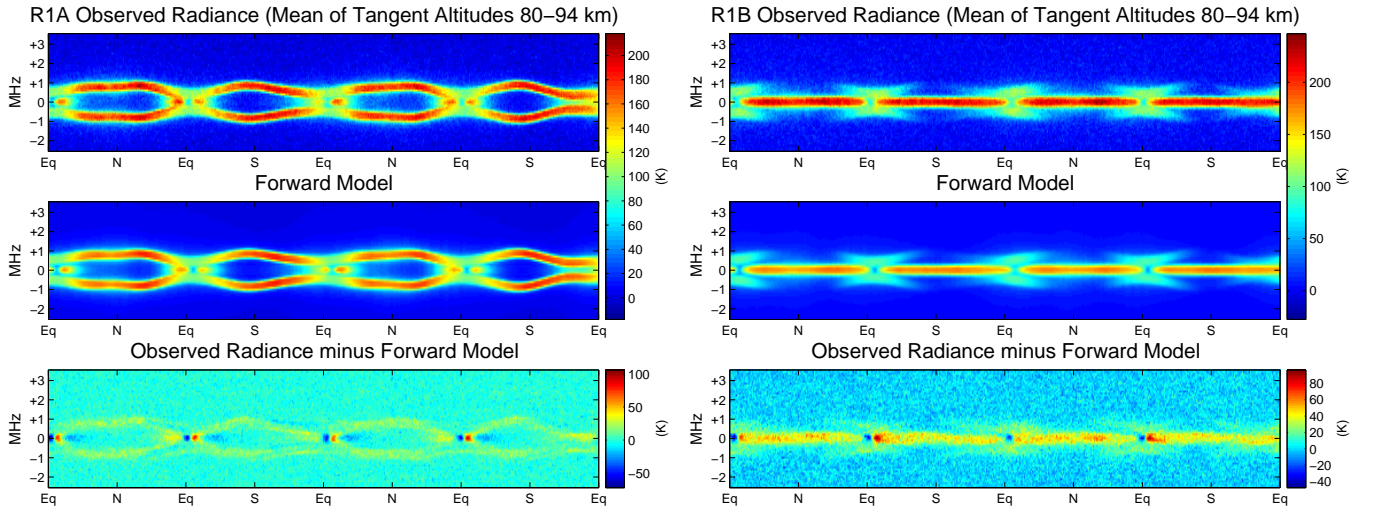

Fig. 5. Top panels show averages of measurements (R1A on left, R1B on right) with tangent points above 80 km, for two orbits from September 1, 2004. The middle panels are corresponding forward model calculations produced by using the atmospheric state retrieved from the MLS data. At high latitudes, $\mathcal{B}_{\text{geo}}$ is nearly normal to the earth's surface and R1A ($\hat{H}$ horizontal) sees the $\sigma_\pm$ lines while R1B ($\hat{H}$ vertical) sees the π line. Residuals (bottom panels) in the line centers may be due to the limited degrees of freedom in the thermospheric temperature profile of the current MLS retrievals. Residuals are worse for the π line, which saturates higher than the σ lines.
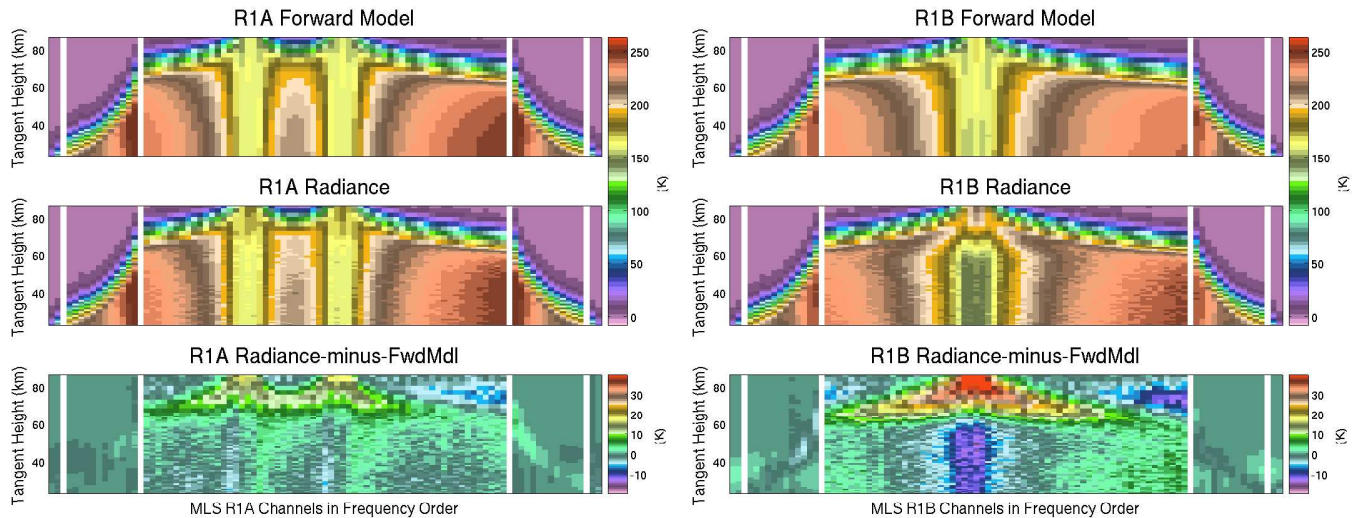
Fig. 6.   These figures show R1A (left) and R1B (right) measured radiances, forward model radiances and their difference from a temperature retrieval for data from September 1, 2004, poleward of 70N. All MLS R1A and R1B channels are displayed in frequency order. In the center of each panel, 61 DACS channels cover 59 MHz. The intermediate sub-panels each contain 12 filterbank channels, which have bandwidths increasing from 8 MHz in the center to 96 MHz at the outside. The narrow strips on the outsides of each panel are each two 500-MHz wide channels, centered 1750 MHz and 3350 MHz from the line center. The $\hat{H}$ vector of R1B is close to the direction of the geomagnetic field, $\mathcal{B}_{geo}$, so we see the π line in R1B. We see the two σ lines, linearly polarized, in R1A.

[12] W. G. Read and Z. Shippony, "EOS MLS forward model algorithm theoretical basis document," Jet Propul. Lab., Pasadena, CA, Tech. Rep. JPL D-18130, March 30 2004. [Online]. Available: http://mls.jpl.nasa.gov

[13] W. Gautschi, "Handbook of mathematical functions," ser. 5.5, M. Abramowitz and I. Stegun, Eds.   National Bureau of Standards, 1972, equations 7.1.3 and 7.1.4.

[14] Z. Shippony and W. G. Read, "A highly accurate Voigt function algorithm," *J. Quant. Spectrosc. Radiat. Transfer*, vol. 50, pp. 635–646, 1993.

[15] P. W. Rosenkranz, "Shape of the 5 mm oxygen band in the atmosphere," *IEEE Transaction on Antennas and Propagation*, vol. AP-23, no. 4, pp. 498–506, July 1975.

[16] ——, Personal Communication, 2002, M.I.T. Research Laboratory of Electronics.

[17] H. M. Pickett, "General rotation and relaxation matrix: Its properties, M dependence, and relation to experiment," *Journal of Chemical Physics*, vol. 61, p. 1923, September 1974.

[18] B. J. Drouin, 2004, personal communication.

[19] M. Tretyakov, G. Y. Golubiatnikov, V. Parshin, M. Koshelev, S. Myasnikova, A. Krupnov, and P. Rosenkranz, "Experimental study of the line mixing coefficient for 118.75 GHz oxygen line," *J. Mol. Spectrosc.*, vol. 223, no. 1, pp. 31–38, 2004.

[20] C. E. Barton, "International geomagnetic reference field: The seventh generation," *J. Geomag. Geoelectr.*, no. 49, pp. 123 – 148, 1997.

[21] M. Mandea *et al.* (2000, 26 May) International Geomagnetic Reference Field - epoch 2000 revision of the IGRF for 2000 - 2005. [Online]. Available: http://www.ngdc.noaa.gov/IAGA/wg8/igrf.html

[22] R. E. Cofield and P. C. Stek, "EOS microwave limb sounderGHz optics design and field-of-view calibration," *IEEE Trans. Geosci. Remote Sensing: The EOS Aura mission*, 2005, this issue.

Michael J. Schwartz began his undergraduate education at Deep Springs College, received his B.A. in Physics from Carleton College in 1985 and his Ph. D. in Physics from Massachusetts Institute of Technology in 1998. His thesis, supervised by Prof. D.H. Staelin, involved atmospheric remote sensing with millimeter-wave oxygen lines. He was on the research staff of the MIT Research Laboratory of Electronics in 1999, where he contributed to the development of an aircraft-based atmospheric sounding package. In 2000, he joined the Microwave Limb Sounding group at the Jet Propulsion Laboratory. His responsibilities have included the development of digital autocorrelator spectrometer hardware and processing algorithms for the EOS-MLS instrument, oversight of the MLS temperature and geopotential height data products, and development of the polarized forward model for Zeeman-split oxygen lines.